

# Prompt2SegCXR: Prompt to Segment All Organs and Diseases in Chest X-rays

Abduz Zami<sup>1\*</sup>, Shadman Sobhan<sup>2</sup>, Rounaq Hossain<sup>3</sup>, Md. Sawran Sorker<sup>4</sup>,  
Mohiuddin Ahmed<sup>5</sup>, Md. Redwan Hossain<sup>6</sup>

<sup>1\*,5</sup>*Department of Computer Science & Engineering,  
Rajshahi University of Engineering & Technology, Rajshahi-6204, Bangladesh*

<sup>2</sup>*Department of Electrical and Electronic Engineering,  
Bangladesh University of Engineering and Technology, Dhaka-1000, Bangladesh*

<sup>3,4</sup>*Bachelor of Medicine and Bachelor of Surgery,  
Shaheed Suhrawardy Medical College, Sher-E-Bangla Nagar, Dhaka-1207*

<sup>6</sup>*Department of Biomedical Engineering,  
Bangladesh University of Engineering and Technology, Dhaka-1000, Bangladesh*

---

## Abstract

Image segmentation plays a vital role in the medical field by isolating organs or regions of interest from surrounding areas. Traditionally, segmentation models are trained on a specific organ or a disease, limiting their ability to handle other organs and diseases. At present, few advanced models can perform multi-organ or multi-disease segmentation, offering greater flexibility. Also, recently, prompt-based image segmentation has gained attention as a more flexible approach. It allows models to segment areas based on user-provided prompts. Despite these advances, there has been no dedicated work on prompt-based interactive multi-organ and multi-disease segmentation, especially for Chest X-rays. This work presents two main contributions: first, generating doodle prompts by medical experts of a collection of datasets from multiple sources with 23 classes, including 6 organs and 17 diseases, specifically designed for prompt-based Chest X-ray segmentation.

---

\*Corresponding author.

*Email addresses:* [abduz.zami@gmail.com](mailto:abduz.zami@gmail.com) (Abduz Zami<sup>1</sup>),  
[shadmansobhan114@gmail.com](mailto:shadmansobhan114@gmail.com) (Shadman Sobhan<sup>2</sup>), [rounaq.bd@gmail.com](mailto:rounaq.bd@gmail.com) (Rounaq Hossain<sup>3</sup>), [sawran100@gmail.com](mailto:sawran100@gmail.com) (Md. Sawran Sorker<sup>4</sup>), [mohiuddin@cse.ruet.ac.bd](mailto:mohiuddin@cse.ruet.ac.bd) (Mohiuddin Ahmed<sup>5</sup>), [redwanhossain6333@gmail.com](mailto:redwanhossain6333@gmail.com) (Md. Redwan Hossain<sup>6</sup>)

Second, we introduce Prompt2SegCXR, a lightweight model for accurately segmenting multiple organs and diseases from Chest X-rays. The model incorporates multi-stage feature fusion, enabling it to combine features from various network layers for better spatial and semantic understanding, enhancing segmentation accuracy. Compared to existing pre-trained models for prompt-based image segmentation, our model scores well, providing a reliable solution for segmenting Chest X-rays based on user prompts.

*Keywords:* Image segmentation, Chest X-ray, Multi-organ segmentation, Multi-disease segmentation, Prompt-based segmentation, Prompt2SegCXR

---

## 1. Introduction

Chest X-ray is a medical imaging system that helps to capture internal organs like lungs, hearts, bones, etc. which cannot be seen with bare eyes. Thus it helps to detect various severe diseases like Pneumonia, Tuberculosis, Pleural Effusion, Bronchitis, etc. [1, 2]. However, segmenting a specific organ from a single chest X-ray containing all the chest organs and disease-affected regions might be difficult especially if that organ or affected region is smaller than other organs. Image segmentation enables the precise identification and isolation of anatomical structures. Thus segmentation helps accurately detect and assess diseases [3].

There are several limitations in the manual or human-annotated segmentation process. The first problem is that it is not generalized, meaning every single chest X-ray has to be segmented separately. This leads to an overall slow process. Also as the work is tiresome, there is a possibility of reduced efficiency [4]. Secondly, for humans, it is not easy to segment tiny, subtle features precisely as these are challenging for the human eye, such as small nodules or micro-calcifications in medical images. To solve all the mentioned problems, computer-based image segmentation methods using deep learning are widely used [5]. Deep learning-based segmentation leads to faster, more generalized, and precise segmentation [6, 7].

Machine learning is a type of statistical algorithm that can learn without definite instructions. Deep learning, a subset of machine learning, is an algorithm that helps computers learn from large amounts of data. It uses neural networks, which are inspired by the way the human brain works. These networks are made up of layers of tiny units, called neurons, that work together to understand patterns in data. The more data it gets, the better it performs.

Deep learning is making a big difference in healthcare, especially in diagnosing diseases [8, 9, 10]. Neural networks can learn from large collections of medical images, like X-rays and CT scans. Regular computer programs are not very good at understanding images, but deep learning models, especially Convolutional Neural Networks (CNNs), are designed for understanding images. CNNs can quickly and accurately find patterns or problems in medical images. Applying deep learning whether in image segmentation or disease classification helps doctors make faster and more accurate diagnoses, which means patients get the right treatment on time. It also reduces the chances of human error. Overall, deep learning makes healthcare smarter and more efficient, improving patient care and saving lives [11].

In the medical field, image segmentation plays a crucial role by helping doctors see specific areas more clearly, such as organs, tissues, or tumors in X-rays, MRIs, or CT scans. Biomedical image segmentation analyzes medical images to detect and highlight areas of concern, like finding a tumor’s exact size and shape. This makes it easier for doctors to diagnose diseases, plan surgeries, and monitor treatments more accurately. By identifying specific regions in an image, segmentation helps in faster and more reliable decision-making. It reduces the chances of human error and ensures that the right area is treated or examined. Overall, image segmentation improves the quality of patient care by making medical imaging clearer, more precise, and easier to analyze [12],[13].

Traditionally, most deep learning-based image segmentation methods are not properly generalized as they aim to segment only a specific organ like lungs, hearts, etc., or a particular disease. However, a situation may arise when a generalized segmentation model is required which can segment any organ or disease a doctor requires. This motivates researchers to develop multi-organ or disease segmentation models for their work [14].

In Natural Language Processing (NLP), large, pre-trained models that serve as a base for a wide range of downstream NLP tasks are called Foundation Models. These models are trained on massive datasets, often involving billions of parameters, and can be fine-tuned for specific tasks such as text classification, machine translation, question answering, and more. Their capability to generalize tasks can be highly enhanced by Prompt Engineering which is hand-crafted text to prompt the language model to generate a valid textual response for the task at hand [15, 16, 17].

So in this work, motivated by multi-organ and multi-disease segmentation and prompt-based input, we are introducing a new paradigm called Interac-

tive Segmentation which leads to generalized image segmentation. Various diseases require image segmentation of various organs. Prompt to Segmentation requires the original chest X-ray and the prompt(doodle), an image that marks the region of interest of the given chest X-ray. The output will be the desired segmented chest X-ray.

Our main contributions are as follows.

- To the best of our knowledge, this is the first doodle prompt-based multi-organ and multi-disease segmentation work for chest X-rays.
- Doodle prompts were created by the medical experts for three datasets that contain 23 classes that include multiple organs and diseases.
- A Dual input segmentation model is proposed that takes the original Chest X-ray image and a doodle input. Then segments the original image based on doodle input.
- The proposed model is a very lightweight segmentation model (with only 8M parameters) that outperformed state-of-the-art models. This model incorporates depthwise separable and pointwise convolution blocks, a residual connection, and an attention module Squeeze-and-Excitation (SE) block.
- Multi-stage fusion is combined for feature fusion at different levels.

The rest of the paper is structured as follows: Section 2 presents a comprehensive review of related works and analyzes existing research gaps. Section 3 discusses the dataset, model architecture. In section 4 we explore the experimental setup which includes different hyperparameter tunings, and evaluation metrics employed in our study. Section 5 presents our experimental results, and compares the results between our model and other models. The paper concludes with a summary of our findings and potential future directions in Section 6.

## 2. Literature Review

Image segmentation is one of the fundamental image processing techniques along with image classification and object detection. Through segmentation, the region of interest is separated from background objects. One of the earliest techniques of image segmentation was region growing. This

technique starts with a seed pixel and recursively adds neighboring pixels with similar properties (such as intensity or color) to form a coherent region. Steven [18] reviewed region growing systems and their role in pictorial segmentation. Besides the mentioned technique, some of the other methods were used for segmentation like thresholding [19], canny edge detection [20], clustering [21]. However, all these techniques were widely used before the rise of deep learning.

The Convolutional Neural Network (CNN) proposed by Lecun et al. [22] revolutionized the field of computer vision. Full Convolutional Networks (FCN) proposed by Long et al. [23] set a new standard for end-to-end semantic segmentation which built the foundation layer of U-Net, a specialized medical image segmentation model, proposed by Ronneberger et al. [24].

Popular medical image segmentation models like U-Net, V-Net [25], Attention U-Net [26], Deeplab [27], Mask R-CNN [28], SegNet [29] are generally used for a specific segmentation task like heart segmentation or lung segmentation etc. with single input. However, for more convenience, multi-organ segmentation has grabbed the attention of researchers to improve existing segmentation works.

For multi-organ segmentation, Liu et al. [30] presented a method for delineating posterior ribs, anterior ribs, and clavicles automatically using a fully convolutional DenseNet (FC-DenseNet) as a pixel classifier. For loss function, they used pixel-weighted loss. Wang et al. [31] took one step further by segmenting the clavicle, anterior rib, posterior rib, and all bones. They proposed Multitask Dense Connection U-Net (MDU-Net) for segmenting the aforementioned organs. Also to force the network to learn the background features, they proposed a mask encoding mechanism. Jie et al. [32] introduced Mask R-CNN for instance segmentation of lung fields, heart, and clavicles. Kholiavchenko et al. [33] improved the performance of lung fields, heart, and clavicle segmentation by providing organ contour information. Wang et al. [34] proposed Multi-objective Segmentation Method for chest X-rays based on Collaborative Learning from Multiple Partially Annotated Datasets (called: MSM-CLMPAD). Their model can accurately segment ribs, clavicles, heart, and lung fields, from chest X-ray images. Compared to multi-organ segmentation, it will be more beneficial if instead of segmenting all organs every time, the model can segment an organ based on user input or prompt. This interactive multi-organ segmentation leads to versatility, efficiency, and flexibility.

Even though segmentation is mostly related to organ separation, seg-

mentation is also used for disease identification. An important application of disease segmentation was demonstrated by Havaei et al. [35] who used segmentation on brain tumours. Campello et al. [36] in their work presented the results of the Multi-Centre, Multi-Vendor and Multi-Disease Cardiac Segmentation (M&Ms) Challenge.

In computer vision applications, CLIP (Contrastive Language-Image Pre-training) [37], ALIGN (A Large-scale Image and Noisy-text embedding) [38], Flamingo [39], BLIP (Bootstrapping Language-Image Pretraining) [40] are some of the models that combine both image and text base modality. Segment Anything Model (SAM) by Meta AI revolutionized the field of prompt-based image segmentation [41]. The strength of SAM lies in its interactive segmentation: the model segments the target following the user-given prompts, such as a point, a bounding box, or free text-like descriptions. However, the inadequate performance of SAM in medical image segmentation led to SAM-Med2D by Cheng et al. [42]. To convert SAM into SAM-Med2D, the SAM model was fine-tuned using 4.6M images and 19.7M masks from public and private datasets. An alternate approach was taken by Wu et al. [43] who instead of fine-tuning, proposed the Medical SAM Adapter (Med-SA). Med-SA incorporates domain-specific medical knowledge into the segmentation model using a light yet effective adaptation technique. Jun et al. [44] took a unique approach, proposing MedSAM, a foundation model that enables universal medical image segmentation. Wu et al. [45] introduced a new model called "One-Prompt Segmentation" which combines the strengths of one-shot and interactive methods. Besides the models that accept image-based prompts, many models are being developed that work with text-based prompts. SegCLIP, developed by Luo et al. [46], works with text-based prompts for segmentation.

In summary, these studies show promising results in the field of multiple organ and disease segmentation and prompt-based medical image segmentation. However, there exists a few research gaps. There is no Chest X-Ray focused interactive segmentation method for all organs and diseases. Also, multi-disease segmentation models are very limited, especially a method that combines both multi-disease and multi-organ segmentation for Chest X-Ray is nowhere to be found according to the best of our knowledge along with a dedicated dataset. Our work focuses on filling the existing gaps.

### 3. Methodology

A dual-input segmentation model, Prompt2SegCXR, was developed to segment specific regions in chest X-rays using doodle prompts. Chest X-rays and segmentation masks were sourced from different datasets. prompts were created by medical expert authors of this research. The model’s architecture was designed with a custom DPRconvSE block incorporating SE attention for feature extraction, along with multi-level fusion in the encoder and decoder. Features were upscaled in the decoder and combined with skip connections to generate precise segmentation masks.

#### 3.1. Dataset Description

The original Chest X-rays were collected from three different datasets. The first source was the Japanese Society of Radiological Technology (JSRT) dataset [47], which contained only the Chest X-rays and no masks. The segmentation masks for the JSRT dataset were collected from the work by Ginneken et al. [48], which contained organ-wise segmentation. From the JSRT dataset, we selected 150 chest X-ray images for each of the following classes: Right Clavicle, Heart, Right Lung, Left Clavicle, and Left Lung.

The second source for the Chest X-rays was the VinDr-RibCXR Dataset [49], which also contained masks, but only for ribs. We took 100 Chest X-rays and their corresponding Rib masks from this dataset.

The final dataset, from which the Chest X-rays were collected, was the Shenzhen Hospital, China dataset [50]. Disease-wise segmentation masks for the remaining classes were provided by this dataset. A maximum of 50 samples per class was taken from this dataset.

Our dataset consisted of 23 classes, including both organs and diseases. The six organ classes were: Right Clavicle, Right Lung, Left Clavicle, Left Lung, and Rib. The remaining 17 classes were diseases, which included Apical Thickening, Calcified lymph node, Calcified Nodule, Cavity, Pleural Effusion, Miliary, Severe Infiltrate (Consolidation), Linear Density, Small Infiltrate (non-linear), Retraction, Clustered Nodule (2mm-5mm part), Adenopathy, Pleural Thickening (non-apical), Calcification (other than nodule or lymph node), Moderate Infiltrate (non-linear), Thickening of interlobar fissure, and Single Nodule (non-calcified).

Each image belonging to a certain class in our dataset had an original Chest X-ray (CXR) and a corresponding segmentation mask.

The number of images belonging to each class whether it is CXR or prompt or mask is shown in Figure 1

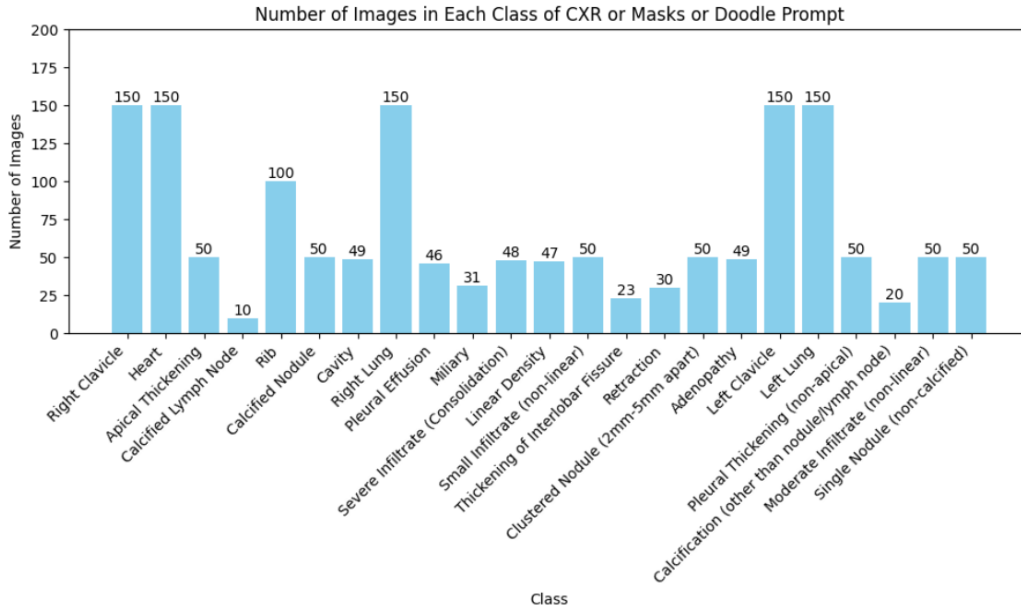


Figure 1: Number of Images in Each Class of CXR or Masks or Doodle Prompt

### 3.2. Prompt Preparation

The doodle prompts were carefully crafted by the medical experts on our team. Using Microsoft Image Viewer, they annotated chest X-rays (CXRs) to highlight specific organs or disease-affected regions. The prompts were then refined by isolating the annotated pixel range, assigning them their intended color, and setting all other pixels to zero for clarity and precision. The prepared prompts are available with the necessary information to map them with the original datasets at <https://www.kaggle.com/datasets/abduzzami/prompt2segcxr-dataset>.

### 3.3. Pre-Processing

Several pre-processing techniques were applied to enhance the input images for our model so that it can be segmented easily. The preprocessing techniques applied in this work were cropping, resizing & grayscale conversion, histogram equalization, and normalization.

At first, cropping was applied to certain images that met the criteria. Some of the masks were very small and had a high chance that the model would not be able to properly generate their mask. That’s why cropping was used. The non-zero pixels in the mask represent the area of interest. smallest bounding box that contains all non-zero pixels in the mask was calculated. A padding value of 100 pixels was used which expanded the bounding box so that the area of interest had a margin around it. Finally, it was ensured that the cropped bounding box was square. Then, if the boundary box covered half the area, the mask was already large enough, so cropping was skipped.

After that, all the images and prompts were converted to the image size of (256,256). In addition, they were converted to grayscale images.

We applied histogram equalization to improve the distribution of pixel intensities across the image. This technique effectively stretched the contrast, making visual features more prominent.

We normalized the original image and the mask image. We generated a unique value for each of the classes. We assigned the unique value to all the non zero pixel values of a particular doodle of a chest x-ray belonging to a certain class.

#### *3.4. Model Architecture*

In this work one of our major contributions was the introduction of Prompt2SegCXR, a lightweight architecture designed to segment specific regions of a Chest X-ray based on a given prompt. Our proposed model utilized various custom blocks with an attention module. The architecture of our model along with used custom blocks are shown in Figure 2

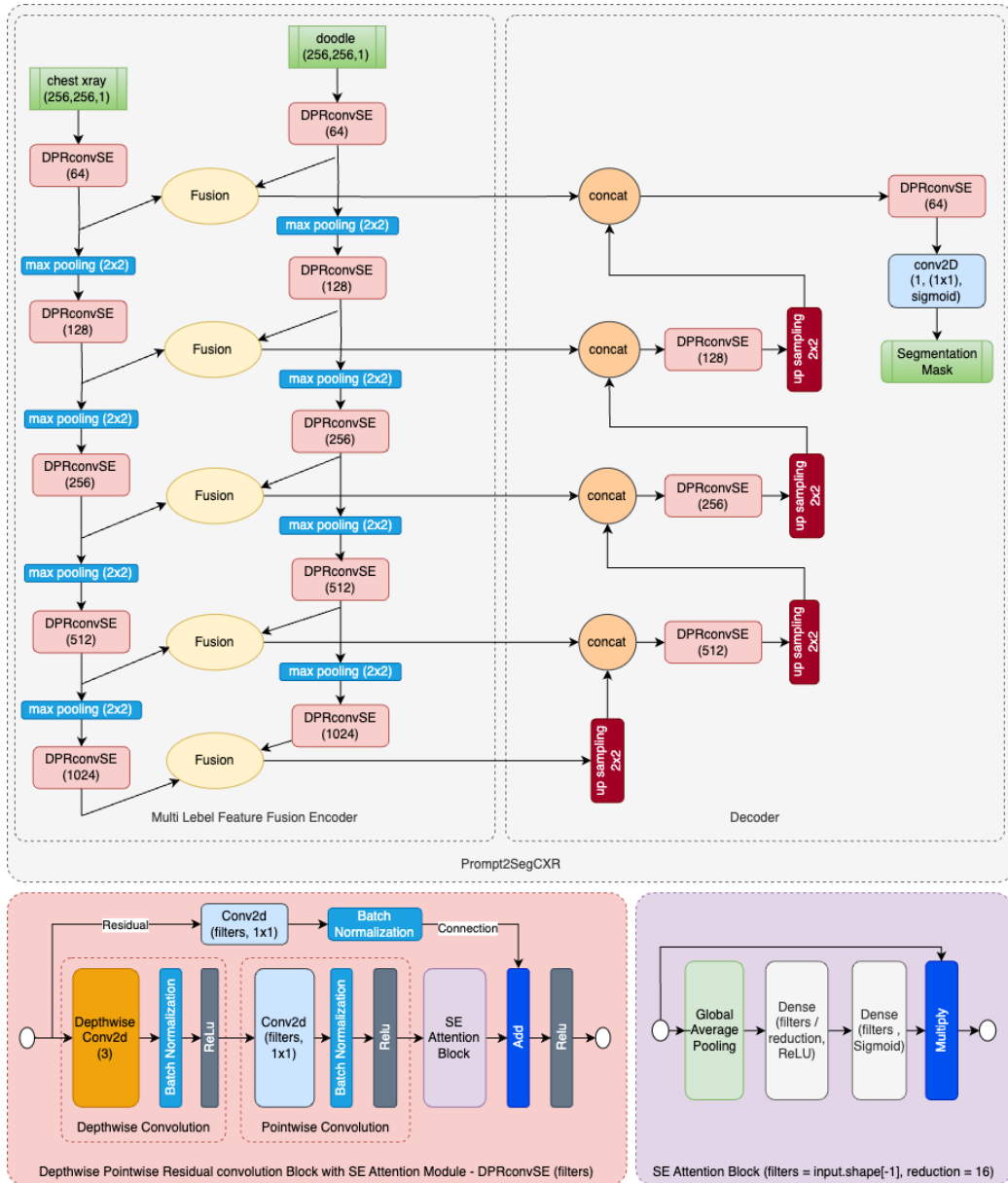


Figure 2: Prompt2SegCXR Model Architecture

### 3.4.1. DPRconvSE Block

The encoder and decoder of our segmentation model had a custom convolution block called DPRconvSE (Depthwise Pointwise Residual convolution

block with SE attention module). This block employed a 3x3 depthwise convolution, followed by batch normalization and ReLU activation. A 1x1 pointwise convolution, along with another batch normalization and ReLU activation layer, is then applied afterwards. Subsequently, an SE (Squeeze-and-Excitation) attention module was employed and added to a residual connection from the input, which passes through a 1x1 pointwise convolution layer with batch normalization. The added result was then passed through a ReLU activation function, which was the output of the DPRconvSE block.

#### 3.4.2. SE attention module

This SE (Squeeze-and-Excitation) attention module was first proposed by Hu et al. [51]. The SE attention module we implemented in the DPRconvSE block, applies global average pooling to the input features, followed by two fully connected layers with ReLU and sigmoid activations. Then multiply it by the input to form the output.

#### 3.4.3. Encoder

The encoder takes two single-channel inputs: the original chest X-ray and a prompt. Both inputs go through the same processing stages. In the first stage, each input is processed by a DPRconvSE block with 64x64 filters, and their outputs are combined using a fusion block.

The resulting features were then passed through four more stages, each consisting of 2x2 max pooling and a DPRconvSE block. In each stage, the filter size of the DPRconvSE block doubles, reaching 1024x1024 in the final stage. At every stage, the outputs of the DPRconvSE block for both inputs were fused using separate fusion blocks.

All five outputs from these fusion blocks were then passed to the decoder.

In summary, the encoder utilized DPRconvSE blocks for feature extraction, 2x2 max pooling for downsampling, and multi-level fusion to combine features from the chest X-ray and prompt at various stages of processing in an integrated way. The fusion blocks integrated the features from the same stage for both inputs, ensuring effective combination before the decoder step.

#### 3.4.4. Decoder

The decoder received five inputs from the encoder. Starting with the output from stage 5, the features are upsampled using a 2x2 kernel and concatenated with the features from the stage 4 fusion block. This combined

output was then processed through a DPRconvSE block with a 512x512 kernel.

This process is repeated for two more stages. In each stage, the features were upsampled, concatenated with the corresponding features from the previous fusion block, and passed through a DPRconvSE block. As the process continues, the filter size of the DPRconvSE block was halved, and upsampling was done using a 2x2 kernel.

In the final stage, the upsampled features were concatenated with the features from the stage 1 fusion block. The combined features were then passed through a DPRconvSE block with a 64x64 filter size, followed by a 1x1 convolution. Finally, a sigmoid activation function generated the output mask.

In summary, the decoder blocks primarily utilized the DPRconvSE block for feature extraction, concatenation to combine features from various stages, and upsampling to increase spatial resolution.

The overall working algorithm is explained in Algorithm 1.

---

**Algorithm 1** Prompt2SegCXR Model with Dual Inputs

---

- 1: **Input:**
  - 2:     $I$ : Image Input of shape (256, 256, 1).
  - 3:     $D$ : Doodle Input of shape (256, 256, 1).
  - 4: **Output:**
  - 5:     $M$ : Segmentation mask of shape (256, 256, 1).
  - 6: **Step 1: Define DPRconvSE Block**
  - 7:    **Input:** Feature map  $x$ , filters  $f$ , kernel size  $k = 3$ , activation  $\sigma = \text{ReLU}$ .
  - 8:    Apply Depthwise Convolution with  $k \times k$  kernel and Batch Normalization.
  - 9:    Apply Pointwise Convolution with  $f$  filters and Batch Normalization.
  - 10:    Apply Squeeze-and-Excitation (SE) Block:
  - 11:      Compute global average pooling on  $x$ .
  - 12:      Dense layer with  $f/16$  units and ReLU activation.
  - 13:      Dense layer with  $f$  units and Sigmoid activation.
  - 14:      Multiply SE weights with  $x$ .
  - 15:    Add residual connection between input  $x$  and SE output.
  - 16:    **Output:** Transformed feature map.
  - 17: **Step 2: Define Image and Doodle Encoder**
  - 18:    **Input:** Input image  $X$  of shape (256, 256, 1).
  - 19:    At each scale, apply:
  - 20:      DPRconvSE block with filter sizes: [64, 128, 256, 512, 1024].
  - 21:      MaxPooling operation for downsampling.
  - 22:    **Output:**            Feature maps from multiple scales:  
                  conv1, conv2, conv3, conv4, conv5.
  - 23: **Step 3: Fuse Features from Image and Doodle Encoders**
  - 24:    Extract feature maps conv1–conv5 from both  $I$  and  $D$ .
  - 25:    Fuse feature maps at each scale using element-wise concatenation:
  - 26:      fusion1 = Concat(image\_conv1, doodle\_conv1).
  - 27:      fusion2 = Concat(image\_conv2, doodle\_conv2).
  - 28:      ...
  - 29: **Step 4: Decoder Path (Upsampling and Skip Connections)**
  - 30:    Start with fused feature map fusion5:
  - 31:      Apply Upsampling by  $2 \times 2$ .
  - 32:      Concatenate with fusion4 (skip connection).
  - 33:      Apply DPRconvSE with 512 filters.
  - 34:    Repeat for fusion3, fusion2, fusion1:
  - 35:      Upsample, concatenate, and apply DPRconvSE at each scale.
  - 36: **Step 5: Generate Segmentation Output**
  - 37:    Apply a  $1 \times 1$  Convolution with Sigmoid activation on the final decoder layer.
  - 38:    Output the segmentation mask  $M$ .
-

## 4. Experimental Setup

The success of a deep learning model depends heavily on the careful design and execution of the experimental setup. In this section, we outline the various steps taken to prepare, train, and evaluate our segmentation model. This involves addressing data imbalances, employing robust cross-validation techniques, tuning hyperparameters for optimal performance, selecting appropriate evaluation metrics, and leveraging computational resources effectively. Each component of the setup was crucial in ensuring the model’s reliability, efficiency, and accuracy.

### 4.1. Handling Class Imbalance

To address the class imbalance in the dataset, we applied the random oversampling technique. This method works by increasing the number of samples in the minority classes by randomly duplicating existing samples until all classes have the same number of samples. This ensured that the dataset was balanced, allowing the model to learn features from all classes equally during training. As a result, the risk of the model favoring majority classes was reduced, improving its overall performance and reliability. This oversampling was applied to only on the train-validation set after splitting the dataset into train-validation and test sets.

### 4.2. Cross-Validation

A 5-fold cross-validation strategy was employed to ensure our model’s robustness and reliability. The dataset was initially split into training/validation and testing sets in an 80:20 ratio such a way that every class of data is divided into that ratio. The training/validation set was divided into 5 equally sized subsets (folds). In each iteration, 1 fold served as the validation set, while the remaining 4 folds were used for training the model. This process was repeated 5 times, ensuring that each fold was used as the validation set exactly once.

Each fold was trained for 20 epochs with a batch size of 16, leading to a total of 100 epochs across all 5 folds. This training process mitigated the risk of over-fitting by exposing the model to various data distributions. The performance metrics from each fold were averaged to give an overall measure of the model’s effectiveness.

### 4.3. Hyperparameter Tuning

To achieve optimal performance and efficient training, we carefully tuned several hyperparameters. The initial learning rate was set to 0.001, and a learning rate reduction strategy was employed where, if the validation Dice coefficient remained constant for five consecutive epochs, the learning rate was reduced to 20% of its current value. This process continued until the learning rate reached a minimum value of  $1 \times 10^{-9}$ . To prevent overfitting, an early stopping criterion was implemented, where training was halted if the validation Dice coefficient did not improve for 10 consecutive epochs. Additionally, model checkpointing was used during training to save the model’s weights whenever an improvement in the validation Dice coefficient was observed, ensuring the best-performing model configuration was preserved for final evaluation.

### 4.4. Evaluation Metrics

To assess the model’s performance, we employed the following metrics:

1. *Dice Coefficient*: The Dice coefficient [52] is used to measure the similarity between the predicted and ground truth segmentation masks. It is calculated as:

$$Dice = \frac{2 \cdot |X \cap Y|}{|X| + |Y|} \quad (1)$$

where  $X$  and  $Y$  are the ground truth and predicted masks, respectively, and  $|\cdot|$  denotes the number of elements in each set.

2. *Jaccard Index*: The Jaccard index [53], also called Intersection over Union (IoU), measures the overlap between two sets. It is defined as:

$$Jaccard = \frac{|X \cap Y|}{|X \cup Y|} \quad (2)$$

where  $X$  and  $Y$  are the ground truth and predicted masks.

3. *Area Under the Curve (AUC)*: The AUC [54] evaluates the model’s ability to distinguish between positive and negative samples. It represents the area under the Receiver Operating Characteristic (ROC) curve.
4. *Binary Accuracy*: Binary accuracy [55] measures the percentage of correctly classified pixels.

#### 4.5. Loss Function

The Dice coefficient loss was used as the optimization objective. It is defined as:

$$DiceLoss = 1 - DiceCoefficient \quad (3)$$

By minimizing this loss, the model was encouraged to maximize the Dice coefficient, which improves segmentation accuracy.

#### 4.6. Machine Configuration

This study was conducted using the computational resources provided by Kaggle’s GPU-accelerated platform [56]. A Kaggle Notebook environment equipped with two NVIDIA Tesla T4 GPUs, each offering 16GB of GDDR6 memory and 2,560 CUDA cores, was utilized.

### 5. Results & Discussion

The scores achieved by our model were compared with other state-of-the-art methods on the segmentation task. The comparison focused on Dice, Jaccard, AUC, and Accuracy, as well as the model’s ability to generalize across different datasets and handle variability in the input images. All the scores presented in this paper were obtained by averaging the scores from three independent runs.

#### 5.1. Scores Obtained by Our Model

Since the dataset included both organ and disease categories, we conducted training in three different configurations: (I) using the entire dataset, (II) using only the organ images, and (III) using only the disease images. The results from training on the entire dataset are presented in Table 1, the results from training on only the organs are shown in Table 2 and the results from training and evaluating on the diseases, excluding those on which our model did not achieve attractive results, are provided in Table 3. Most of the classes got an attractive score, though a few classes like Linear Density, Thickening of Interlobar Fissure, Calcified Lymph Node, and Single Nodule (non-calcified) got a less attractive score than others.

The superior performance of the Prompt2SegCXR model can be attributed to its combination of advanced architectural components. The use of depth-wise pointwise convolutions allowed the model to efficiently extract features

Table 1: Results of Training and Evaluating on Full Dataset

Class	Dice	Jaccard	AUC	Accuracy
Right Clavicle	86.32	76.12	91.76	98.36
Heart	92.87	86.73	94.58	95.99
Apical Thickening	64.96	48.54	83.77	98.60
Calcified Lymph Node	38.69	24.00	72.47	98.76
Rib	81.18	66.96	87.09	90.10
Calcified Nodule	76.36	65.89	85.65	99.47
Cavity	66.32	49.68	86.29	98.61
Right Lung	95.80	91.96	96.38	98.49
Pleural Effusion	60.55	43.83	77.81	93.81
Miliary	82.50	70.75	91.12	95.86
Severe Infiltrate (Consolidation)	89.61	81.31	95.17	97.24
Linear Density	19.83	11.28	57.51	97.64
Small Infiltrate (non-linear)	58.21	41.48	73.61	94.10
Thickening of Interlobar Fissure	34.75	22.96	64.89	97.58
Retraction	44.41	31.04	68.14	93.36
Clustered Nodule (2mm-5mm apart)	84.61	73.71	96.07	99.39
Adenopathy	79.09	65.96	89.32	96.78
Left Clavicle	78.60	65.06	84.46	97.89
Left Lung	94.09	88.95	95.01	98.32
Pleural Thickening (non-apical)	64.66	47.87	86.99	98.64
Calcification (other than nodule/lymph node)	50.20	34.41	76.97	97.92
Moderate Infiltrate (non-linear)	68.40	53.60	80.52	94.94
Single Nodule (non-calcified)	39.90	27.38	71.18	98.39
All	81.62	70.38	88.92	97.03

Table 2: Results of Training and Evaluating on only Organs

Class	Dice	Jaccard	AUC	Accuracy
Right Clavicle	89.73	81.58	94.28	98.70
Heart	94.22	89.11	96.59	98.62
Right Lung	97.24	94.64	98.76	98.97
Rib	78.92	65.21	87.15	90.35
Left Clavicle	91.02	83.62	95.10	98.82
Left Lung	97.13	94.43	98.69	99.10
All	92.47	86.45	96.00	97.57

Table 3: Results of Training and Evaluating on only Diseases excluding few

Class	Dice	Jaccard	AUC	Accuracy
Apical Thickening	70.80	55.40	87.59	98.34
Calcified Lymph Node	30.14	17.75	59.67	95.90
Calcified Nodule	65.37	49.25	79.88	99.31
Cavity	72.02	57.26	91.10	98.56
Pleural Effusion	62.61	45.69	80.84	94.54
Miliary	81.24	68.52	88.94	95.50
Severe Infiltrate (Consolidation)	87.53	78.46	92.68	97.12
Small Infiltrate (non-linear)	64.42	47.91	78.32	94.72
Retraction	52.73	35.89	73.58	91.20
Clustered Nodule (2mm-5mm apart)	77.61	63.77	92.86	98.65
Adenopathy	71.68	56.45	83.41	96.23
Pleural Thickening (non-apical)	60.13	44.11	81.73	98.37
Moderate Infiltrate (non-linear)	66.05	49.85	81.03	93.67
All	73.08	57.63	85.63	96.86

while reducing computational complexity, enabling it to handle intricate patterns and variations in the input data. The inclusion of residual connections helped mitigate issues related to vanishing gradients, ensuring that important feature maps are preserved throughout the network. Squeeze-and-Excitation (SE) attention modules further enhanced feature selection by focusing on the most relevant areas of the input, emphasizing significant details while suppressing less informative ones. The multi-stage fusion mechanism played a crucial role by aggregating features from different levels of abstraction, effectively integrating low-level details with high-level context. This approach allowed the model to maintain accuracy across diverse and complex datasets, where simple feature extraction might fail. Together, these elements enable the Prompt2SegCXR model to achieve robust and precise segmentation, making it particularly effective in challenging scenarios where standard models might underperform.

The performance of the Prompt2SegCXR model varied across different classes, highlighting both its strengths and limitations. Prompt2SegCXR showed a little bit less attractive scores for diseases than the organs. This is a possibility due to the region of segmentation in diseases being very small. So the doodle generation was also challenging for the diseases, particularly for Linear Density. Linear Density affected regions are very small in size and of line shape. Few other disease classes, such as Thickening of Interlobar

Fissure, and Calcified Lymph Node, exhibited lower scores due to similar reasons.

Additionally, imbalances in the dataset, particularly in classes with fewer samples, limited the model’s ability to generalize effectively, despite the application of oversampling techniques. Overlapping visual characteristics between certain classes, such as Pleural Effusion and Adenopathy, also contributed to misclassifications. The quality of the user-provided prompts further influences the model’s performance; ambiguous or imprecise prompts can reduce segmentation accuracy. While the lightweight architecture ensures computational efficiency, it may lack the depth required to capture highly complex or nuanced features compared to more extensive state-of-the-art models.

The graphical view of the performance of our model is shown in Figure 3.

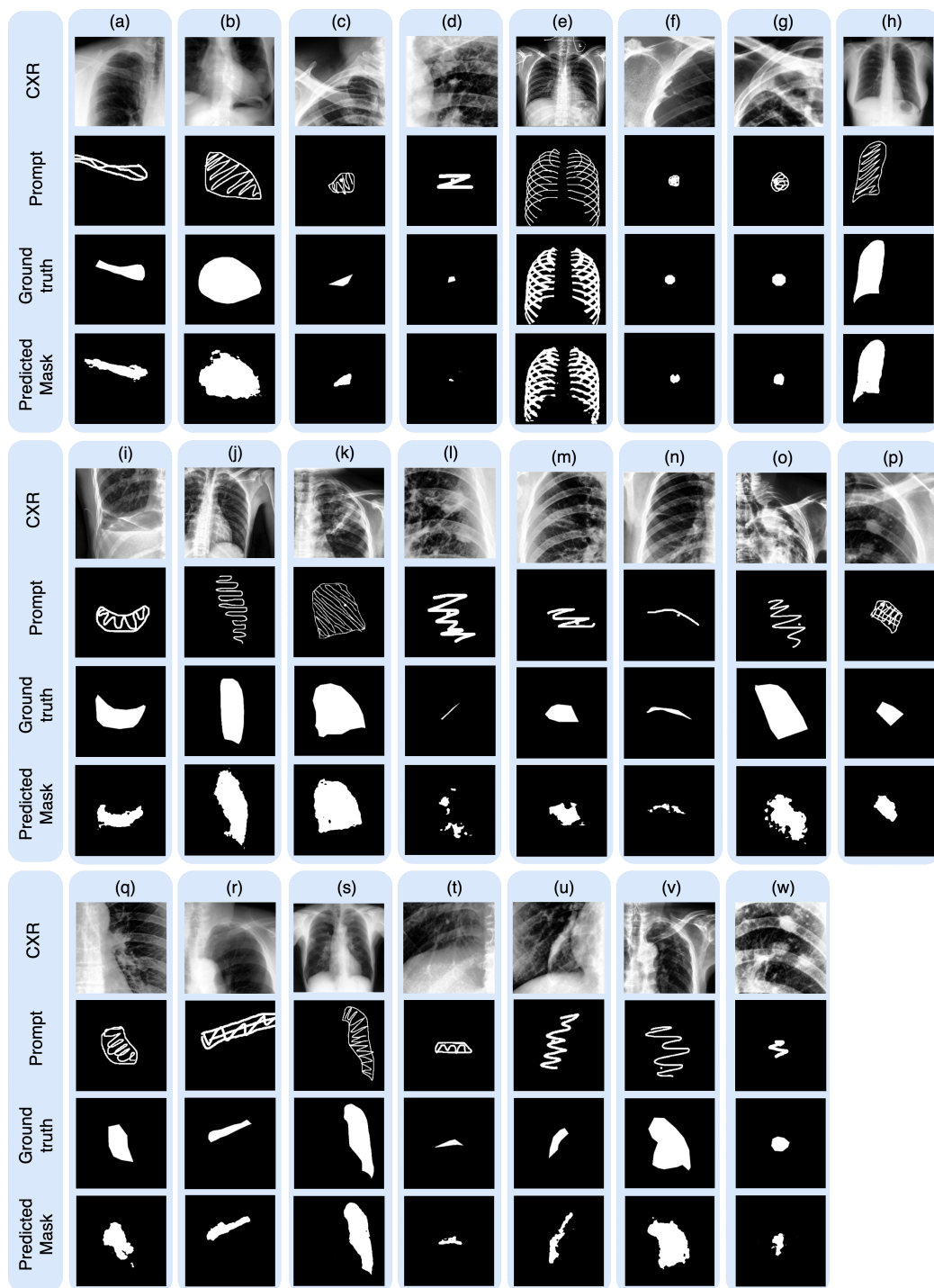


Figure 3: Prediction Samples of Our Model across all the classes (a) Right Clavicle (b) Heart (c) Apical Thickening (d) Calcified lymph node (e) Rib (f) Calcified Nodule (g) Cavity (h) Right Lung (i) Pleural Effusion (j) Miliary (k) Severe Infiltrate (Consolidation) (l) Linear Density (m) Small Infiltrate (non linear) (n) Thickening of interlobar fissure (o) Retraction (p) Clustered Nodule (2mm-5mm apart) (q) Adenopathy (r) Left Clavicle (s) Left Lung (t) Pleural Thickening (non-apical) (u) Calcification (other than nodule lymphnod) (v) Moderate Infiltrate (non-linear) (w) Single Nodule (non-calcified)

### 5.2. Performance of Ablation Experiments

We conducted a series of ablation experiments to assess the incremental contributions of various architectural components and techniques to the segmentation performance. Starting with the baseline network, which utilized a multi stage feature fusion technique, we progressively incorporated the point-wise and depthwise convolutions, squeeze-and-excitation attention module, residual connections, and a random oversampling technique to address class imbalance. The results are presented in Table 4.

The baseline model, incorporating pointwise convolutions, achieved a Dice score of 66.94% and an jaccard index of 51.79%. The addition of depthwise convolutions improved feature extraction efficiency, leading to a Dice score of 78.69%. Incorporating the squeeze-and-excitation attention module enhanced the network’s ability to focus on significant regions, increasing the Dice score to 79.32%. Adding residual connections further facilitated gradient flow, resulting in a Dice score of 79.92%. Finally, addressing class imbalance through random oversampling yielded the best performance, achieving a Dice score of 81.62%, a Jaccard index of 70.38%, and an accuracy of 97.03%. These findings underscore the critical role of combining architectural advancements with effective data-balancing techniques to achieve robust segmentation performance.

Table 4: Performance metrics for various model configurations, showcasing the impact of progressively integrating Pointwise Convolution (PW), Depthwise Convolution (DW), Squeeze-and-Excitation attention module (SE), Residual Connections (RC), and Random Oversampling (ROS) on segmentation accuracy

Cases	Dice	Jaccard	AUC	Accuracy
Baseline+PW+PW	66.94	51.79	87.08	93.32
Baseline+DW+PW	78.69	66.68	91.03	96.09
Baseline+DW+PW+SE	79.32	67.37	90.69	96.27
Baseline+DW+PW+SE+RC	79.92	68.45	<b>92.42</b>	96.33
Baseline+DW+PW+SE+RC+ROS (proposed)	<b>81.62</b>	<b>70.38</b>	88.92	<b>97.03</b>

### 5.3. Comparison with Other Works

To the best of our knowledge, this was the first doodle prompt-based Chest X-ray segmentation work, there was no existing model that could be trained on the dataset and be compared to our work. So we compared the performance of our model with variations of the Segment Anything Model (SAM). At present SAM-based medical image segmentation models

are the most prominent general-purpose, prompt-based segmentation models. As prompt they require BBox (Bounding Box). Table 5 compares our model(trained on the full dataset) with SAM-based medical image segmentation models (zero-shot prediction).

Table 5: Comparison of Prompt2SegCXR Model and few SAM based zero-shot models

Models	Prompt	Dice	Jaccard	AUC	Accuracy
SAM	BBox	71.25	58.16	84.09	92.64
MedSAM	BBox	74.82	62.98	83.74	95.38
SAM Med 2D	BBox	73.66	61.37	85.95	95.28
Ours	Doodle	<b>81.62</b>	<b>70.38</b>	<b>88.92</b>	<b>97.03</b>

The Prompt2SegCXR model outperformed other SAM-based medical image segmentation models in zero-shot prediction due to its effective multi-stage fusion architecture. The choice of a doodle-based prompt rather than a bounding box also enhanced its performance by capturing detailed, region-specific features. These elements allowed the model to achieve better segmentation accuracy even with fewer parameters. Other models may have struggled to match the performance of Prompt2SegCXR because they were not specifically trained on the diverse set of diseases present in our dataset. This lack of targeted training limited their ability to handle the unique characteristics and complexities associated with these specific medical conditions, reducing their segmentation accuracy and preventing them from fully leveraging the required information for precise diagnosis.

## 6. Conclusions and Future Works

This study introduces a dataset containing doodle prompts for Chest X-ray (CXR) segmentation, which includes a variety of organs and diseases, along with a unique doodle prompt mechanism. The dataset covers 6 organs and 17 diseases, making it ideal for developing models that can segment multiple organs and diseases. Along with the dataset, we present Prompt2SegCXR, a lightweight segmentation model that uses user-provided prompts (doodles) to segment organs and diseases interactively. Unlike traditional models, Prompt2SegCXR can handle multiple organs and diseases with high accuracy and precision. Its lightweight design ensures it performs efficiently, even in resource-limited environments like hospitals. Compared

to current state-of-the-art models, Prompt2SegCXR outperforms in both accuracy and precision, making it a promising tool for improving clinical workflows. Together, the prompt dataset and Prompt2SegCXR set a new standard for prompt-based segmentation, with potential applications beyond Chest X-rays.

While this work provides a strong foundation for prompt-based segmentation in medical imaging, there are several areas for future research and improvement. Despite its strengths, the model’s performance on disease segmentation was slightly lower than for organs, especially in some particular diseases, primarily due to challenges in segmenting small or complex regions. Challenges in creating prompts for small and complex shapes of affected regions, dataset imbalances and overlapping visual features also contributed to reduced performance. Future works can focus on these issues to be solved. These also include expanding Prompt2SegCXR to other medical imaging types like CT scans, MRIs, and ultrasounds to enhance its generalization. Additionally, applying transfer learning to fine-tune the model for specific diseases and integrating it into existing clinical workflows would improve its real-world applicability. By addressing these areas, future research can enhance prompt-based segmentation, leading to more flexible and accurate diagnostic tools.

## **CRedit Author Statement**

## **Acknowledgement**

## **References**

- [1] H. P. McAdams, E. Samei, J. Dobbins III, G. D. Tourassi, C. E. Ravin, Recent advances in chest radiography, *Radiology* 241 (2006) 663–683.
- [2] N. Subramanian, O. Elharrouss, S. Al-Maadeed, M. Chowdhury, A review of deep learning-based detection methods for covid-19, *Computers in Biology and Medicine* 143 (2022) 105233.
- [3] P. Aggarwal, R. Vig, S. Bhadoria, C. Dethe, Role of segmentation in medical imaging: A comparative study, *International Journal of Computer Applications* 29 (2011) 54–61.

- [4] C. E. Cardenas, J. Yang, B. M. Anderson, L. E. Court, K. B. Brock, Advances in auto-segmentation, in: *Seminars in radiation oncology*, volume 29, Elsevier, 2019, pp. 185–197.
- [5] I. R. I. Haque, J. Neubert, Deep learning approaches to biomedical image segmentation, *Informatics in Medicine Unlocked* 18 (2020) 100297.
- [6] H. Seo, M. Badieli Khuzani, V. Vasudevan, C. Huang, H. Ren, R. Xiao, X. Jia, L. Xing, Machine learning techniques for biomedical image segmentation: an overview of technical aspects and introduction to state-of-art applications, *Medical physics* 47 (2020) e148–e167.
- [7] H. R. Roth, C. Shen, H. Oda, M. Oda, Y. Hayashi, K. Misawa, K. Mori, Deep learning and its application to medical image segmentation, *Medical Imaging Technology* 36 (2018) 63–71.
- [8] R. Miotto, F. Wang, S. Wang, X. Jiang, J. T. Dudley, Deep learning for healthcare: review, opportunities and challenges, *Briefings in bioinformatics* 19 (2018) 1236–1246.
- [9] S. S. Nisha, M. N. Meeral, Applications of deep learning in biomedical engineering, in: *Handbook of deep learning in biomedical engineering*, Elsevier, 2021, pp. 245–270.
- [10] M. Kim, C. Yan, D. Yang, Q. Wang, J. Ma, G. Wu, Deep learning in biomedical image analysis, in: *Biomedical information technology*, Elsevier, 2020, pp. 239–263.
- [11] F. Shaik, Y. Rajesh, N. A. Gudur, J. K. Dash, Deep cnn in healthcare, in: *Deep Learning in Biomedical Signal and Medical Imaging*, CRC Press, 2024, pp. 221–236.
- [12] X. Liu, L. Song, S. Liu, Y. Zhang, A review of deep-learning-based medical image segmentation methods, *Sustainability* 13 (2021) 1224.
- [13] Y. Mo, Y. Wu, X. Yang, F. Liu, Y. Liao, Review the state-of-the-art technologies of semantic segmentation based on deep learning, *Neuro-computing* 493 (2022) 626–646.
- [14] X. Liu, L. Qu, Z. Xie, J. Zhao, Y. Shi, Z. Song, Towards more precise automatic analysis: a comprehensive survey of deep learning-based multi-organ segmentation, *arXiv preprint arXiv:2303.00232* (2023).

- [15] J. White, Q. Fu, S. Hays, M. Sandborn, C. Olea, H. Gilbert, A. Elnashar, J. Spencer-Smith, D. C. Schmidt, A prompt pattern catalog to enhance prompt engineering with chatgpt, arXiv preprint arXiv:2302.11382 (2023).
- [16] J. Wang, Z. Liu, L. Zhao, Z. Wu, C. Ma, S. Yu, H. Dai, Q. Yang, Y. Liu, S. Zhang, et al., Review of large vision models and visual prompt engineering, *Meta-Radiology* (2023) 100047.
- [17] Y. Liu, G. Deng, Z. Xu, Y. Li, Y. Zheng, Y. Zhang, L. Zhao, T. Zhang, K. Wang, Y. Liu, Jailbreaking chatgpt via prompt engineering: An empirical study, arXiv preprint arXiv:2305.13860 (2023).
- [18] S. W. Zucker, Region growing: Childhood and adolescence, *Computer graphics and image processing* 5 (1976) 382–399.
- [19] R. Kohler, A segmentation system based on thresholding, *Computer Graphics and Image Processing* 15 (1981) 319–338.
- [20] J. Canny, A computational approach to edge detection, *IEEE Transactions on pattern analysis and machine intelligence* (1986) 679–698.
- [21] G. B. Coleman, H. C. Andrews, Image segmentation by clustering, *Proceedings of the IEEE* 67 (1979) 773–785.
- [22] Y. LeCun, L. Bottou, Y. Bengio, P. Haffner, Gradient-based learning applied to document recognition, *Proceedings of the IEEE* 86 (1998) 2278–2324.
- [23] J. Long, E. Shelhamer, T. Darrell, Fully convolutional networks for semantic segmentation, in: *Proceedings of the IEEE conference on computer vision and pattern recognition*, 2015, pp. 3431–3440.
- [24] O. Ronneberger, P. Fischer, T. Brox, U-net: Convolutional networks for biomedical image segmentation, in: *Medical image computing and computer-assisted intervention—MICCAI 2015: 18th international conference, Munich, Germany, October 5-9, 2015, proceedings, part III* 18, Springer, 2015, pp. 234–241.
- [25] F. Milletari, N. Navab, S.-A. Ahmadi, V-net: Fully convolutional neural networks for volumetric medical image segmentation, in: *2016 fourth international conference on 3D vision (3DV)*, Ieee, 2016, pp. 565–571.

- [26] O. Oktay, J. Schlemper, L. L. Folgoc, M. Lee, M. Heinrich, K. Misawa, K. Mori, S. McDonagh, N. Y. Hammerla, B. Kainz, et al., Attention u-net: Learning where to look for the pancreas, arXiv preprint arXiv:1804.03999 (2018).
- [27] L.-C. Chen, G. Papandreou, I. Kokkinos, K. Murphy, A. L. Yuille, Deeplab: Semantic image segmentation with deep convolutional nets, atrous convolution, and fully connected crfs, *IEEE transactions on pattern analysis and machine intelligence* 40 (2017) 834–848.
- [28] K. He, G. Gkioxari, P. Dollár, R. Girshick, Mask r-cnn, in: *Proceedings of the IEEE international conference on computer vision*, 2017, pp. 2961–2969.
- [29] V. Badrinarayanan, A. Kendall, R. Cipolla, Segnet: A deep convolutional encoder-decoder architecture for image segmentation, *IEEE transactions on pattern analysis and machine intelligence* 39 (2017) 2481–2495.
- [30] Y. Liu, X. Zhang, G. Cai, Y. Chen, Z. Yun, Q. Feng, W. Yang, Automatic delineation of ribs and clavicles in chest radiographs using fully convolutional densenets, *Computer methods and programs in biomedicine* 180 (2019) 105014.
- [31] W. Wang, H. Feng, Q. Bu, L. Cui, Y. Xie, A. Zhang, J. Feng, Z. Zhu, Z. Chen, Mdu-net: A convolutional network for clavicle and rib segmentation from a chest radiograph, *Journal of Healthcare Engineering* 2020 (2020) 2785464.
- [32] J. Wang, Z. Li, R. Jiang, Z. Xie, Instance segmentation of anatomical structures in chest radiographs, in: *2019 IEEE 32nd International Symposium on Computer-Based Medical Systems (CBMS)*, IEEE, 2019, pp. 441–446.
- [33] M. Kholiavchenko, I. Sirazitdinov, K. Kubrak, R. Badrutdinova, R. Kuleev, Y. Yuan, T. Vrtovec, B. Ibragimov, Contour-aware multi-label chest x-ray organ segmentation, *International Journal of Computer Assisted Radiology and Surgery* 15 (2020) 425–436.
- [34] H. Wang, D. Zhang, J. Feng, L. Cascone, M. Nappi, S. Wan, A multi-objective segmentation method for chest x-rays based on collaborative

- learning from multiple partially annotated datasets, *Information Fusion* 102 (2024) 102016.
- [35] M. Havaei, A. Davy, D. Warde-Farley, A. Biard, A. Courville, Y. Bengio, C. Pal, P.-M. Jodoin, H. Larochelle, Brain tumor segmentation with deep neural networks, *Medical image analysis* 35 (2017) 18–31.
  - [36] V. M. Campello, P. Gkontra, C. Izquierdo, C. Martin-Isla, A. Sojoudi, P. M. Full, K. Maier-Hein, Y. Zhang, Z. He, J. Ma, et al., Multi-centre, multi-vendor and multi-disease cardiac segmentation: the m&ms challenge, *IEEE Transactions on Medical Imaging* 40 (2021) 3543–3554.
  - [37] A. Radford, J. W. Kim, C. Hallacy, A. Ramesh, G. Goh, S. Agarwal, G. Sastry, A. Askell, P. Mishkin, J. Clark, et al., Learning transferable visual models from natural language supervision, in: *International conference on machine learning*, PMLR, 2021, pp. 8748–8763.
  - [38] C. Jia, Y. Yang, Y. Xia, Y.-T. Chen, Z. Parekh, H. Pham, Q. Le, Y.-H. Sung, Z. Li, T. Duerig, Scaling up visual and vision-language representation learning with noisy text supervision, in: *International conference on machine learning*, PMLR, 2021, pp. 4904–4916.
  - [39] J.-B. Alayrac, J. Donahue, P. Luc, A. Miech, I. Barr, Y. Hasson, K. Lenc, A. Mensch, K. Millican, M. Reynolds, et al., Flamingo: a visual language model for few-shot learning, *Advances in neural information processing systems* 35 (2022) 23716–23736.
  - [40] J. Li, D. Li, C. Xiong, S. Hoi, Blip: Bootstrapping language-image pre-training for unified vision-language understanding and generation, in: *International conference on machine learning*, PMLR, 2022, pp. 12888–12900.
  - [41] A. Kirillov, E. Mintun, N. Ravi, H. Mao, C. Rolland, L. Gustafson, T. Xiao, S. Whitehead, A. C. Berg, W.-Y. Lo, et al., Segment anything, in: *Proceedings of the IEEE/CVF International Conference on Computer Vision*, 2023, pp. 4015–4026.
  - [42] J. Cheng, J. Ye, Z. Deng, J. Chen, T. Li, H. Wang, Y. Su, Z. Huang, J. Chen, L. Jiang, et al., Sam-med2d, *arXiv preprint arXiv:2308.16184* (2023).

- [43] J. Wu, W. Ji, Y. Liu, H. Fu, M. Xu, Y. Xu, Y. Jin, Medical sam adapter: Adapting segment anything model for medical image segmentation, arXiv preprint arXiv:2304.12620 (2023).
- [44] J. Ma, Y. He, F. Li, L. Han, C. You, B. Wang, Segment anything in medical images, *Nature Communications* 15 (2024) 654.
- [45] J. Wu, M. Xu, One-prompt to segment all medical images, in: *Proceedings of the IEEE/CVF Conference on Computer Vision and Pattern Recognition*, 2024, pp. 11302–11312.
- [46] H. Luo, J. Bao, Y. Wu, X. He, T. Li, Segclip: Patch aggregation with learnable centers for open-vocabulary semantic segmentation, in: *International Conference on Machine Learning*, PMLR, 2023, pp. 23033–23044.
- [47] J. S. of Radiological Technology (JSRT), The standard digital image database of chest radiographs with and without a lung nodule was developed as part of the research activities of the academic committee of the japanese society of radiological technology (jsrt) in 1998 (\*1), supported by the japan radiological society (jrs) and with the cooperation of healthcare facilities in japan and the united states for providing case materials., <http://db.jsrt.or.jp/eng.php>, 1998. Accessed on: 2024-06-15.
- [48] B. van Ginneken, Scr database, 2022. URL: <https://doi.org/10.5281/zenodo.7056076>. doi:10.5281/zenodo.7056076.
- [49] H. C. Nguyen, T. T. Le, H. H. Pham, H. Q. Nguyen, Vindr-ribcxr: A benchmark dataset for automatic segmentation and labeling of individual ribs on chest x-rays, arXiv preprint arXiv:2107.01327 (2021).
- [50] Shenzhen Hospital, Shenzhen hospital x-ray set collected by shenzhen no.3 hospital in shenzhen, guangdong province, china. the x-rays were acquired as part of the routine care at shenzhen hospital., <https://data.lhncbc.nlm.nih.gov/public/Tuberculosis-Chest-X-ray-Datasets/Shenzhen-Hospital-CXR-Set/index.html>, 2021. Accessed on: 2024-06-15.

- [51] J. Hu, L. Shen, G. Sun, Squeeze-and-excitation networks, in: Proceedings of the IEEE conference on computer vision and pattern recognition, 2018, pp. 7132–7141.
- [52] L. R. Dice, Measures of the amount of ecologic association between species, *Ecology* 26 (1945) 297–302. URL: <https://esajournals.onlinelibrary.wiley.com/doi/abs/10.2307/1932409>. doi:<https://doi.org/10.2307/1932409>. arXiv:<https://esajournals.onlinelibrary.wiley.com/doi/pdf/10.2307/1932409>.
- [53] A. H. Murphy, The finley affair: A signal event in the history of forecast verification, *Weather and Forecasting* 11 (1996) 3. doi:10.1175/1520-0434(1996)011<0003:TFAASE>2.0.CO;2.
- [54] J. M. Lobo, A. Jiménez-Valverde, R. Real, Auc: a misleading measure of the performance of predictive distribution models, *Global Ecology and Biogeography* 17 (2008) 145–151. doi:10.1111/j.1466-8238.2007.00358.x.
- [55] Accuracy (trueness and precision) of measurement methods and results - part 1: General principles and definitions, 1994.
- [56] Kaggle, Kaggle: Your home for data science, 2010. URL: <https://www.kaggle.com/>, accessed: 2024-09-06.